chemosensors

MDPI

Article

Optimizing the Heavy Metal Ion Sensing Properties of Functionalized Silver Nanoparticles: The Role of Surface Coating Density

Andrea Rossi [1], Massimiliano Cuccioloni [2,*], Lisa Rita Magnaghi [3], Raffaela Biesuz [3], Marco Zannotti [1,*], Laura Petetta [1], Mauro Angeletti [2] and Rita Giovannetti [1]

[1] School of Science and Technology, Chemistry Division, University of Camerino, 62032 Camerino, Italy
[2] School of Biosciences and Veterinary Medicine, University of Camerino, 62032 Camerino, Italy
[3] Department of Chemistry, University of Pavia, Viale Taramelli 12, 27100 Pavia, Italy
* Correspondence: massimiliano.cuccioloni@unicam.it (M.C.); marco.zannotti@unicam.it (M.Z.); Tel.: +39-0373-403247 (M.C.)

Abstract: We present a colorimetric sensor based on functionalized silver nanoparticles for the detection of metal ions in aqueous solutions. The interaction between the target metal ion and the functionalizing agent triggers the aggregation of these nanoparticles, and the consequent change in optical properties allows the detection/quantification of the analyte. In detail, this work describes the synthesis of AgNPs by a chemical reduction method, and the production of mercaptoundecanoic acid functionalized NPs with different surface densities (multi-, full-, and two partial layers). UV-Vis spectroscopy was used to monitor the functionalization processes, and to investigate the aggregation behavior of each AgNPs@11MUA sensor upon titration with the metal ions of interest, namely Ni^{2+}, Zn^{2+}, Co^{2+}, Cd^{2+}, Mn^{2+}, and Cu^{2+}. The resulting UV-Vis raw data obtained for each layer density were submitted to principal component analysis to dissect the role of the metal ions in NP aggregation and in establishing the sensitivity and selectivity of the AgNPs@11MUA sensor. Interestingly, we observed an increase in sensor sensitivity and selectivity at a lower density of the functionalizing agent on the AgNPs' surface, which results in characteristic colors of the NP suspension upon titration with each metal ion.

Keywords: colorimetric sensor; silver nanoparticles; surface functionalization; metal ions detection

Citation: Rossi, A.; Cuccioloni, M.; Magnaghi, L.R.; Biesuz, R.; Zannotti, M.; Petetta, L.; Angeletti, M.; Giovannetti, R. Optimizing the Heavy Metal Ion Sensing Properties of Functionalized Silver Nanoparticles: The Role of Surface Coating Density. *Chemosensors* **2022**, *10*, 483. https://doi.org/10.3390/chemosensors10110483

Academic Editor: Kien Wen Sun

Received: 20 October 2022
Accepted: 12 November 2022
Published: 15 November 2022

1. Introduction

The progressive development of anthropic activities has contributed to an increase in the environmental levels of several toxic pollutants, such as heavy metal ions, anions, organic compounds, dyes, drugs, pesticides, bacteria, viruses, and gases [1], with hazardous consequences to human health [2]. Great efforts have been devoted to developing analytical methods for their rapid, real-time, sensitive, and selective determination [3]. In this context, recent advances in nanotechnology and materials science have prompted the use of nanoparticles (NPs) [4], quantum dots [5–7], carbon nanotubes [8], graphene [9–11], nano-sheets [12] and other two-dimensional nanomaterials in the field of sensors [10].

In particular, nanoparticle-based colorimetric sensors exhibited promising results in the detection of metallic ions [13], organic dyes [14], drugs [15], pesticides [16], and viruses [17], with their sensing mechanism mainly relying on NP aggregation [18–20]. Their popularity is also growing rapidly due to their ease of fabrication, rapid detection, high sensitivity, and naked-eye sensing [21].

Gold, silver, and copper NPs are the most widely used metallic NPs [22] with unique optical properties due to strong surface plasmon resonance (SPR) [23–25], which is generated by the collective oscillation of electrons at the interface between metal and dielectric [26].

Among these, silver nanoparticles (AgNPs) are largely used as optical sensing materials [27,28] due to their cost-effective properties compared with AuNPs and broader range of applications compared with CuNPs (which cannot be used in aqueous solvents [29]). Most importantly, AgNPs display high values in the molar extinction coefficients in the range 10^8–10^{11} M^{-1} cm^{-1} in their absorption band [30], also known as the surface plasmon absorption band (SPAB), which lies in the range 390–600 nm depending on the shape, dimension, composition, and dielectric constant [31], resulting in an unambiguous color of the colloidal suspension [32,33].

In these aggregation-based sensors, the chromatic variation in the colloidal suspension is triggered by the interaction of the NPs with the analyte of interest [20], which is accompanied by the appearance of a second SPAB at a higher wavelength [34]. In fact, the decrease in the interparticle distance (induced by the nanoparticle aggregation) leads to a strong plasmon coupling between the nearby particles, which in turn causes changes in the plasmon bands and a consequent change in the color of the colloidal solution [35,36].

Although several research articles focus on the identification of the optimal functionalizing agent for the detection/quantification of a given analyte, no studies on the correlation between the sensor behavior and the density of the functionalized layer are currently available. To fill this gap, in this work we report on the synthesis and characterization of AgNPs and the functionalization thereof with different levels of 11MUA. Most importantly, AgNPs@11MUA at different layer densities were individually titrated with a panel of the most common heavy metals ions (namely Ni^{2+}, Zn^{2+}, Co^{2+}, Cd^{2+}, Mn^{2+}, and Cu^{2+}) [37], and the corresponding changes in SPAB were discussed. To further dissect spectral features associated with each AgNPs@11MUA's density layer, a multivariate approach was exploited to compare the effect of the different metal ions, relying on principal component analysis (PCA) directly applied to the SPAB, which could be considered the "chemical fingerprint" of the samples under investigation [38].

2. Materials and Methods

2.1. Materials

Silver nitrate ($AgNO_3$), sodium borohydride ($NaBH_4$), mercaptoundecanoic acid (11MUA), $NiCl_2$, $CoCl_2$, $ZnCl_2$, $CuCl_2$, $MnCl_2$, and $CdCl_2$ were purchased from Sigma-Aldrich (St. Louis, MO, USA). All these chemicals were used as received without further purification. Aqua regia was used to wash all the glassware before being used. Ultrapure water (18.2 μS/cm) produced by Milli-Q® Advantage A10, Merk, was used to prepare all the solutions.

2.2. Synthesis and Surface Functionalization of AgNPs

Functionalized AgNPs were obtained with the same procedure reported in our previous work [13]. Briefly, AgNPs were synthesized by adding 1 mL of freshly prepared water solution of $NaBH_4$ (0.25 M) to 50 mL of $AgNO_3$-containing water solution (0.001 M) and stirred for 30 min. For the functionalization, a specific amount of a stock solution of 11MUA in NaOH-solution (0.6 M, pH = 9) was added to the particle suspension and stirred for 24 h. The exact amount of 11MUA added to each AgNP suspension is reported in Table 1.

Table 1. The number of moles of 11MUA added to the AgNP suspension for the functionalization, corresponding number of 11MUA molecules per nanoparticle, and % of saturation for ML = multi-layer, FL = full-layer, and $PL_{1,2}$ = partial layers, respectively.

11MUA Layer	Mol of 11MUA	11MUA/NP	Saturation %
ML	1.33×10^{-3}	2.42×10^{16}	*multilayer*
FL	1.33×10^{-5}	2.42×10^{14}	100
PL_1	1.33×10^{-7}	2.42×10^{12}	1
PL_2	1.33×10^{-11}	2.42×10^{8}	0.000001

2.3. Characterization of Bare and Functionalized AgNPs

UV-Vis spectra of AgNPs and AgNPs@11MUA at different layer densities and the SPABs observed at each step of the titration were acquired with a Cary 8454 Diode Array System spectrophotometer (Agilent Technologies, Santa Clara, CA, USA).

X-ray diffraction (XRD) of AgNPs was carried out using a custom horizontal Debye–Scherrer diffractometer as described elsewhere [39].

2.4. Colorimetric Response Investigation

The colorimetric response of the AgNPs@11MUA sensor was investigated upon step-wise additions of 10 µL of each metal stock solution (0.1 mM) to the AgNPs@11MUA suspension. SPAB was acquired at each step of titration to build the dose/response curves.

2.5. Morphological Analysis by Scanning Electron Microscopy (SEM)

Field emission scanning electron microscopy (FE-SEM, Sigma 300, Zeiss, Germany) operating at 7 kV, equipped with energy dispersive X-ray spectroscopy (EDX, Quantax, EDS, Bruker, Billerica, MA, USA), was used to evaluate the morphology of AgNPs and AgNPs@11MUA. Samples were prepared as described elsewhere [13].

2.6. Multivariate Data Treatment

UV-Vis spectra were collected at each step of the titration of 11MUA-coated AgNPs with all the metal ions of interest, and the overall dataset was submitted to PCA, applying autoscaling as column pretreatment. This procedure was individually repeated for each layer density. Only the region from 300 to 800 nm was considered, since it was the most informative portion of the spectrum for this investigation. The multivariate data treatment was performed using the open-source software CAT [40].

3. Results and Discussions

3.1. Scanning Electron Microscopy Characterization

AgNPs morphology was revealed by SEM characterization; the particles displayed a spherical distribution, characteristic of AgNPs that possess a SPAB in the range 350–450 nm [41]. Size analysis was performed by ImageJ software on 200 nanoparticles and data were fitted by normal distribution, revealing an average diameter of ~23.07 ± 5.12 nm (Figure 1). The absence of stabilizers, which was necessary to ensure that only 11MUA was bonded on the surface of the particles, caused polydispersity in the NPs' distribution. Upon functionalization, AgNPs retained the same morphology as demonstrated in our previous work [13].

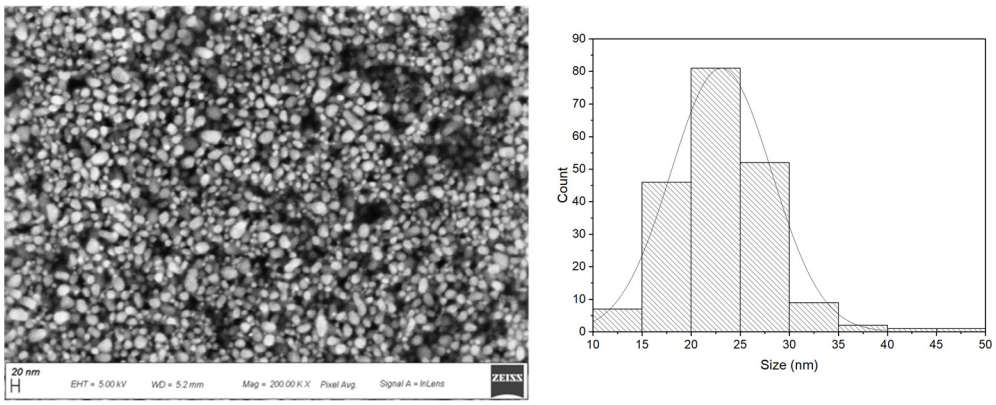

Figure 1. SEM image of AgNPs 11MUA at Mag = 200.00 K× (**left** panel). Particle size distribution (~ 23.07 ± 5.12 nm) obtained by size analysis with ImageJ software (**right** panel).

3.2. Functionalization of AgNPs with Different Layer Densities

The number of 11MUA molecules necessary to form one monolayer functionalization was calculated on the assumption that a maximum of 3 ± 1 molecules of 11MUA can be packed in 1 nm^2 [42]. The surface of the nanoparticles was calculated by size distribution analysis of AgNPs, as described in the Experimental Section. Assuming that all the Ag-ions react to form AgNPs, the number of particles in the colloidal suspension was calculated by Equation (1) [43]:

$$N_{NPs} = \frac{m}{\rho \times 4/3\pi r^3} = 8.06 \times 10^{13} \text{ mol} \quad (1)$$

where "ρ" is the density of the face-centered cubic (fcc) silver (=10.5 g/cm^3), "r" is the mean radius of the particles (11.5 nm = 11.5×10^{-7} cm), and "m" is the mass of silver (0.0054 g). Postulating a spherical distribution of NPs, the surface area *Sa* of the particles was calculated by Equation (2):

$$Sa = N_{NPs} \times s = 1340 \text{ cm}^2 \quad (2)$$

where "N_{NPs}" is the number of NPs previously obtained, and "s" is the surface of NPs obtained by considering the mean radius of NPs in cm^2. Therefore, the amount of 11MUA to obtain a monolayer functionalization can be easily obtained (Sa $\times$ 3 $\times$ MUA/nm^2). Table 1 reports the number of 11MUA molecules per nanoparticle in the different synthesized layers. Specifically, in the full-layer functionalization (FL), 2.42×10^{14} molecules of 11MUA were present on a single nanoparticle, whereas in the multi-layer (ML), the number of 11MUA molecules increased 100-fold. Two different partial layers ($PL_{1,2}$) were synthesized using 2.42×10^{12} and 2.42×10^{8} molecules of 11MUA per NP, respectively.

3.3. Spectrophotometer Characterization of Bare AgNPs and AgNPs@11MUA

The colorless to pale-yellow change after the addition of a reducing agent to the solution containing Ag^+ confirmed the formation of bare silver nanoparticles. The successful formation of AgNPs was further verified by XRD (Figure S5). The addition of a functionalizing agent caused the increase in the color intensity of the AgNP suspension. The SPAB of bare AgNPs showed a strong absorption at 392 nm, characteristic of spherical AgNPs, whereas AgNPs functionalized with different concentrations of 11MUA (Table 1) resulted in a red shift (393–440 nm) of the SPAB due to the interaction between thiol group on the surface of the NPs (Figure 2) [44–46].

3.4. Spectrophotometric Characterization of 11MUA–Metal-Ion Interactions

The interactions between free mercaptoundecanoic acid and different metal ions were investigated by UV-Vis spectroscopy to rule out possible interferences of the metal–ligand complex with the SPAB of AgNP@11MUA. UV-Vis spectra (Figure 3) showed absorption bands at wavelengths below 290 nm for all the investigated metal ions. Interaction between Cu^{2+} and Mn^{2+}, with 11MUA also showing a broad and low-intensity absorbance at 400 nm. Therefore, we could reasonably argue that the individual second SPAB generated upon the interaction between AgNPs@11MUA and the metal ions of interest (M) is mainly attributable to the formation of the AgNPs@11MUA-M lattice.

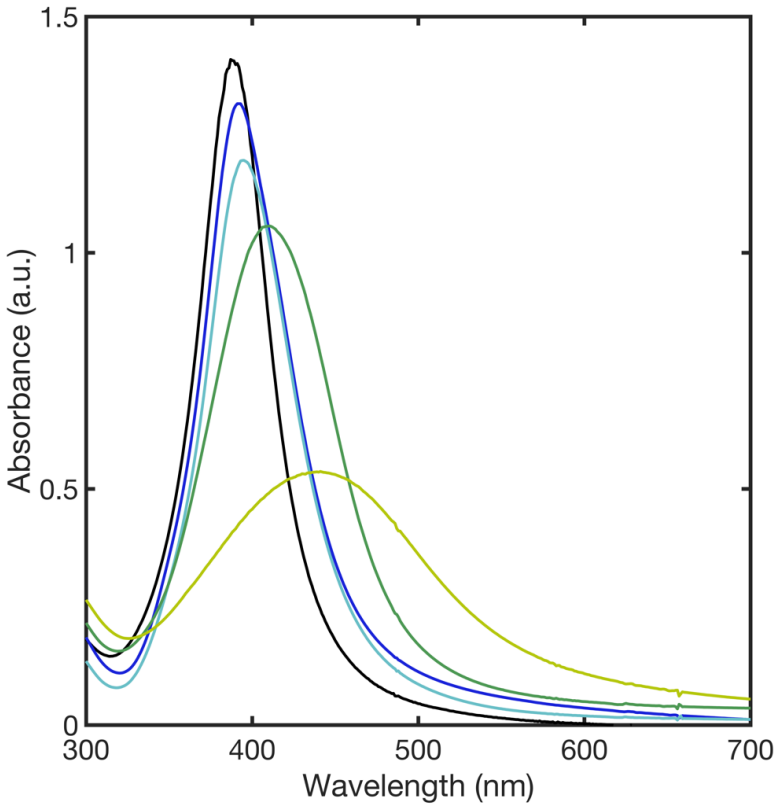

Figure 2. SPAB of the bare AgNPs (black line), and SPABs of AgNPs after the functionalization with a multi-layer (blue line), full layer (cyan line), and two different partial layers, PL_1 (green line) and PL_2 (yellow line), respectively.

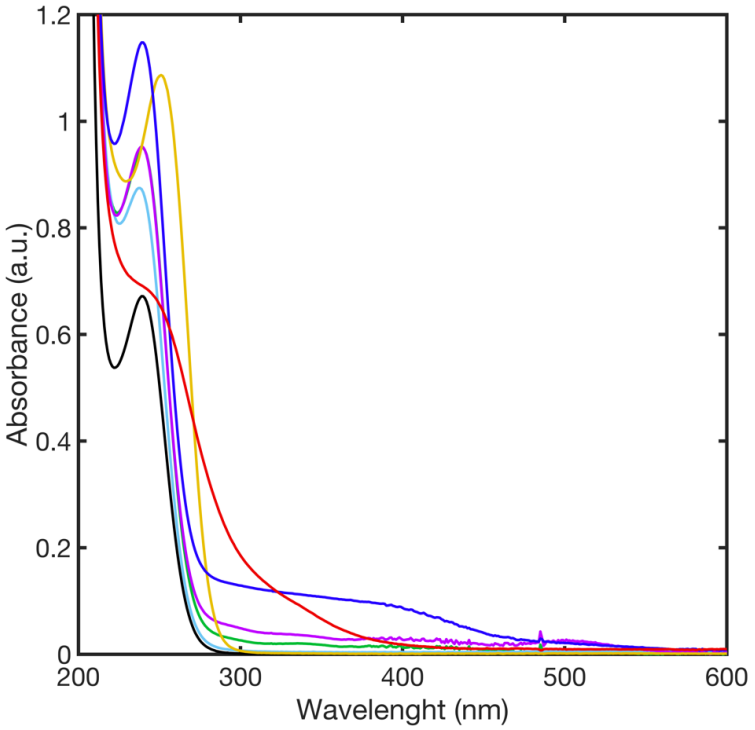

Figure 3. UV-Vis spectra of complexes formed upon the addition of metal ions to the 11MUA in NaOH solution; 11MUA (black line), Ni^{2+} (green line), Mn^{2+} (blue line), Cu^{2+} (red line), Zn^{2+} (cyan line), Co^{2+} (purple line), and Cd^{2+} (yellow line).

3.5. Titration of AgNPs@11MUA with Metal Ions

Specifically, different AgNPs colloidal suspensions with different surface densities (ML, FL, PL_1, and PL_2) were titrated with each metal-ion solution (Ni^{2+}, Zn^{2+}, Cu^{2+}, Cd^{2+}, Co^{2+}, Cr^{2+}) and the consequent aggregation was evaluated by UV-Vis spectroscopy.

3.5.1. ML–AgNPs@11MUA

Upon titration of ML–AgNPs@11MUA with metal ions, the corresponding UV-Vis spectra did not show the appearance of the second SPAB, characteristic of aggregated NPs. Figure 4 shows a representative superimposition of spectra obtained at the highest concentration of tested metal ions and the relationship between absorbance ratio (Abs_{550}/Abs_{420}) and metal-ion concentration.

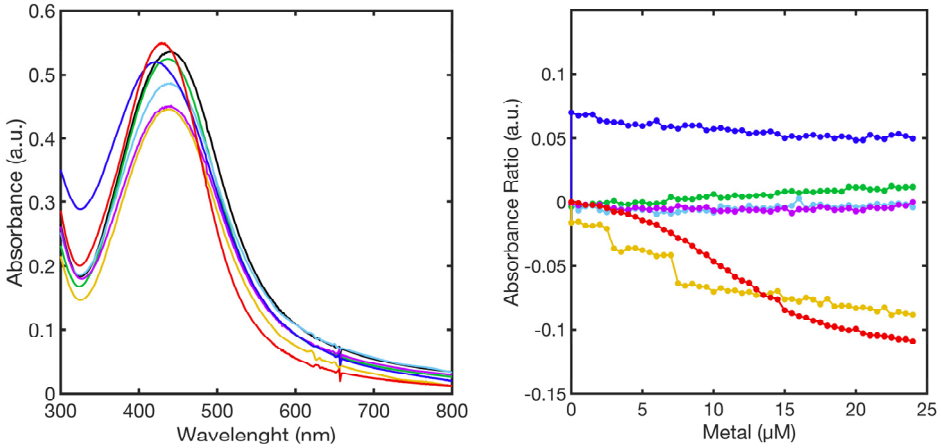

Figure 4. SPABs of ML–AgNPs@11MUA (black line) obtained at the highest concentration of metal ions (**left**-panel); calibration curve showing the relationship between absorbance ratio and metal ion concentration used in the titrations (**right**-panel). Ni^{2+} (green line), Mn^{2+} (blue line), Cu^{2+} (red line), Zn^{2+} (cyan line), Co^{2+} (purple line), and Cd^{2+} (yellow line).

Additional information was obtained by submitting the entire dataset to principal component analysis. In this case, PC1 and PC2 together accounted for 95.70% of the percentage variance. The loadings plot (Figure S1) clearly showed that PC1 represented 85.32% of the spectra variation for the entire region (300–800 nm) whereas PC2 represented 10.38% of variance, which allowed us to distinguish samples with signals in the region below 500 nm, located in the positive part of the axis, from those reporting signals above 500 nm, placed in the negative part of the axes.

In the scores plot (Figure 5), no clear distinction among the different metal ions was observed alongside PC1 or PC2. Nevertheless, when considering metal ions individually, PC1 revealed variations in the UV-Vis spectra upon titration even in the absence of the second SPAB, with a resulting decrease in the score value. The highest effect was observed when Cu^{2+} and Cd^{2+} were added to ML–AgNPs@11MUA, whereas no variation was observed for Mn^{2+}.

The blue shift observed for the SPAB can be rationalized by hypothesizing that, at concentrations of 11MUA far greater than in the FL, the functionalizing agent can form a multilayer due to the formation of either secondary interactions (even layers) or disulfide bonds (odd layers) between the surface-bound 11MUA and free 11MUA [47,48]. The formation of this multilayer was confirmed by the strong change in the SPAB observed upon functionalization, as previously demonstrated for analogous functionalized NPs [49,50].

Based on this assumption, the titration of ML–AgNPs@11MUA with metal ions could promote the formation of Met^{2+}-SH and Met^{2+}-COOH coordination complexes and disrupt the secondary MUA–MUA interactions that stabilize the multilayer, eventually reversing the red shift of the SPAB associated with the formation of the multilayer (Figure 6) [51–53].

Figure 5. PCA score plot for PC1 and PC2 components upon titration of SPABs of ML–AgNPs@11MUA with each metal ion.

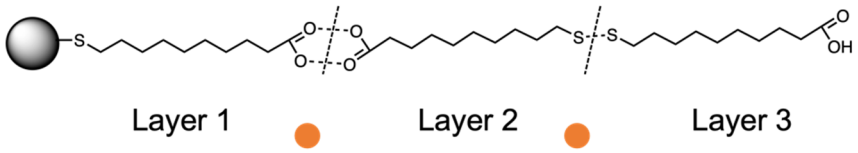

Figure 6. Schematic representation of the multi-layer arrangement for ML–AgNPs@11MUA on the surface of the NPs. ● indicates the metal ions that could disrupt MUA–MUA secondary interactions.

3.5.2. FL–AgNPs@11MUA

The analysis of the SPABs upon titration of FL–AgNPs@11MUA with metal ions revealed a metal-type-dependent aggregation behavior. The comparison of the spectra obtained at the highest concentration of each metal ion showed that FL–AgNPs@11MUA fully aggregated after the addition of 10µM Ni^{2+} and 17 µM of Mn^{2+} and Cd^{2+}. Differently, Zn^{2+}, Cu^{2+}, and Co^{2+} were extremely inactive, as the aggregation of FL–AgNPs@11MUA was not triggered upon additions in the same concentration range (Figure 7, left panel).

The superimposition of titration curves (Abs_{550}/Abs_{414} vs metal concentration) reported in Figure 7, right panel, is representative of the sensor sensitivity to each metal.

In this case too, submitting the entire dataset to PCA, PC1 and PC2 together accounted for an high percentage of variance (90.11%). Specifically, the analysis of the loadings plot (Figure S2), showed that the separation alongside PC1 (62.89%) was mainly attributed to the region of the spectra above 500 nm, with a positive contribution, and to the region between 350 and 450 nm, with a negative contribution; on the other hand, the separation along PC2 was associated with changes in the SPAB at 350 and 450 nm, with a positive contribution.

The scores plot (Figure 8) revealed no significative change in the UV-Vis spectra upon titration with Cu^{2+} and Zn^{2+}. Conversely, PC1 and (only to a minor extent) PC2 score values increased with Co^{2+}, Mn^{2+}, and Cd^{2+} concentrations; this behavior was likely dependent upon the simultaneous decrease in the intensity of the SPABs characteristic of dispersed ML–AgNPs@11MUA, and the broadening of the SPABs (no well-defined second SPAB was observed). Conversely, a different trend was observed for Ni^{2+}, since it was clearly separated alongside PC1, due to a decrease in the signal intensity of dispersed

ML–AgNPS@11MUA at increasing concentrations, and alongside PC2, due to the formation of a second well-defined SPAB [13].

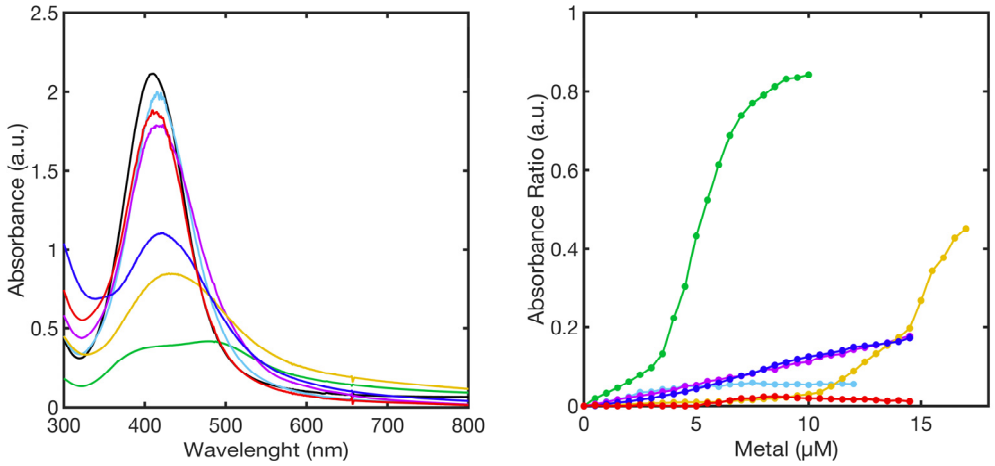

Figure 7. SPABs of FL–AgNPs@11MUA (black line) obtained at the highest concentration of metal ions (**left**-panel); calibration curve showing the relationship between absorbance ratio and metal ion concentration used in the titrations (**right**-panel). Ni^{2+} (green line), Mn^{2+} (blue line), Cu^{2+} (red line), Zn^{2+} (cyan line), Co^{2+} (purple line), and Cd^{2+} (yellow line).

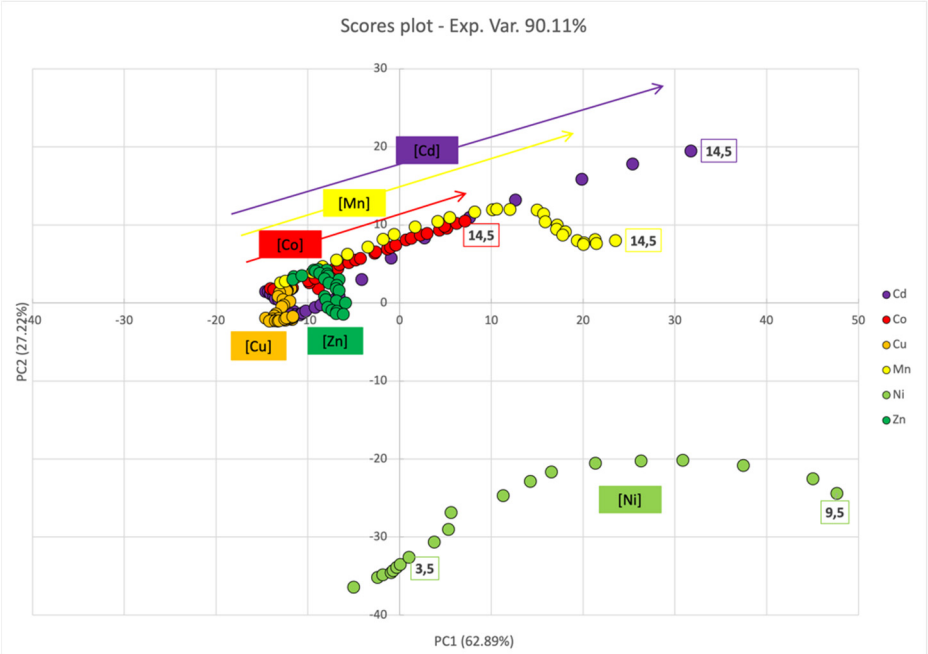

Figure 8. PCA score plot for PC1 and PC2 components upon titration of SPABs of FL–AgNPs@11MUA with each metal ion.

3.5.3. $PL_{1,2}$–AgNPs@11MUA

The interaction between metal ions and partially functionalized AgNPs, namely PL_1 and PL_2 (2×10^{12} and 2×10^8 molecules of 11MUA per NP, respectively), was investigated by UV-Vis spectroscopy upon titrations with each metal ion. Generally, a second SPAB was observed at a higher wavelength, indicating the aggregation of AgNPs. Table 2 summarizes the position of the second SPABs, identified by the deconvolution of the spectra with a lognormal function, for each metal for PL_1 and PL_2, respectively [54,55].

Table 2. Wavelength position of the second SPABs in nm obtained by spectra deconvolution using a lognormal distribution.

Metals Ions	PL_1 SPAB (nm)	PL_2 SPAB (nm)
Zn^{2+}	506	594
Cd^{2+}	560	613
Co^{2+}	531	595
Ni^{2+}	516	568
Mn^{2+}	620	670
Cu^{2+}	537	635

The UV-Vis titration spectra of PL_1-AgNPs@11MUA with each metal ion at the highest concentration, and the corresponding titration curves ($Abs_2{}^{nd}{}_{SPAB}/Abs_{397}$ vs concentration) showed that all metal ions caused the full aggregation of the PL_1-AgNPS@11MUA at ~20 µM of metal ion (Figure 9).

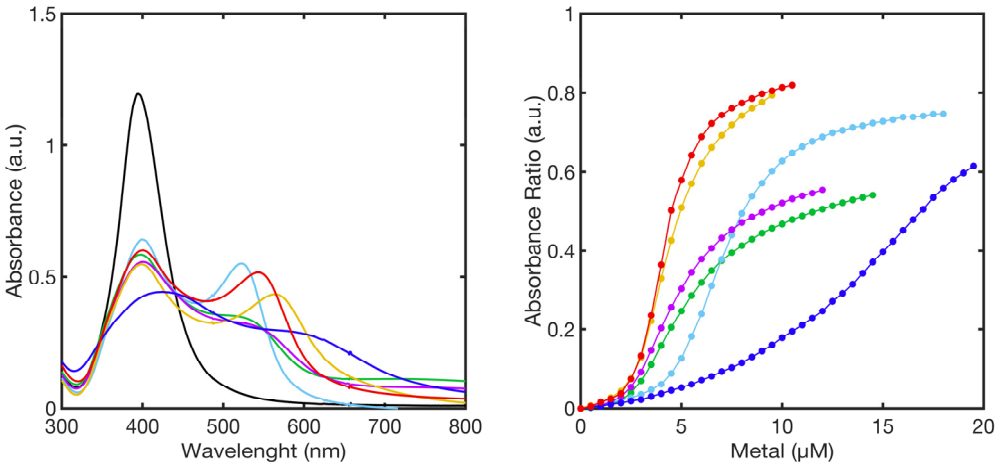

Figure 9. Superimposition of UV-Vis spectra of PL_1-AgNPs@11MUA (black line) obtained at the highest concentration of metal ions (**left**-panel), calibration curve showing the relationship between absorbance ratio and metal concentration used in the titrations (**right**-panel). Ni^{2+} (green line), Mn^{2+} (blue line), Cu^{2+} (red line), Zn^{2+} (cyan line), Co^{2+} (purple line), and Cd^{2+} (yellow line).

All the titration curves showed three major regions: an "initial zone", in which only a few clusters of PL_1-AgNPS@11MUA-M are formed; an "intermediate zone", in which the addition of metal ions caused a strong change in the SPAB resulting in the formation of a superlattice of previously formed PL_1-AgNPS@11MUA-M clusters [56]; and a "pre-saturation zone" in which the superlattice reaches a critical size and collapses. Interestingly, upon individual titration, particular colors were observed for each metal ion (Figure 10).

Considering the multivariate analysis in the case of partial monolayer, PC1 and PC2 accounted for 80.6% of the experimental variance (see loading plot Figure S3). Analyzing the loading plot in Figure S3, alongside PC1 (60.26%), 450 nm emerged as the discriminating wavelength between positive (>450 nm) and negative contributions (<450 nm), whereas PC2 (20.20%) was associated with SPAB broadening (local maxima at approximately 350 nm and 435 nm) and the appearance of signals between 450 and 600. Peak shift and background had a positive contribution, whereas the 450–600 zone had a negative contribution.

The scores plot (Figure 11) showed a shift for all metal ions towards higher PC1 score values by increasing the concentration, due to the decrease and increase in the first and second SPAB, respectively. The shift along the PC1 axis also reflected the behavior of the titration curves reported in Figure 9 (right panel), since it followed the same trend with a higher shift in the "intermediate zone". Additionally, the PC1 score also evidenced that the optimal sensing zone depended on the type of metal ion added to the PL_1-AgNPS@11MUA.

PC2 instead discriminated the metal ions mainly on the position of the second SPAB; in fact, those metal ions that generate secondary well-resolved SPABs (and do not cause a high enlargement of the first SPAB), were placed in the bottom part of the score plot. This behavior was found for Zn^{2+}, Cd^{2+}, and Cu^{2+}. Conversely, those metals that did not show a second well-resolved SPAB, such as Ni^{2+}, Mn^{2+} and, to a lesser extent, Co^{2+}, were in the top part of the plot.

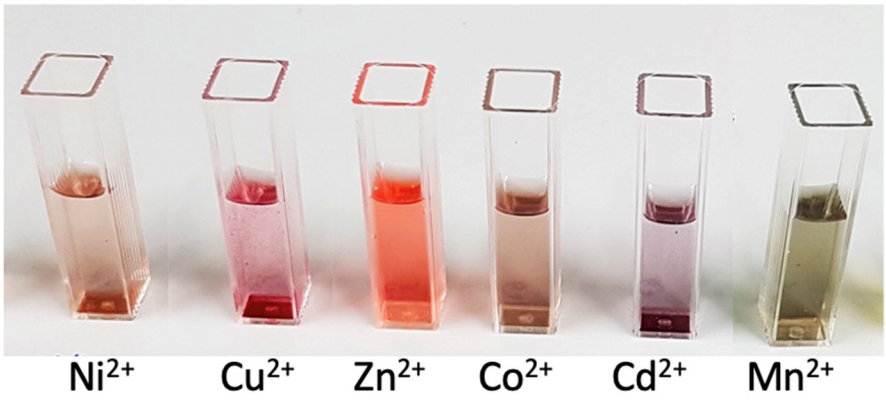

Figure 10. PL_1-AgNPs@11MUA upon the addition of each metal ion at the highest concentration of metal ion added before the collapse.

Figure 11. PCA score plot for PC1 and PC2 components upon titration of SPABs of PL_1-AgNPs@11MUA with each metal ion.

At further lower layer density (2×10^8 molecules of 11MUA per NP, PL_2-AgNPS@11MUA), a shift toward higher wavelengths of the second SPAB was observed with respect to PL_1 (Table 2). As for the other partial layer, the formation of a second well-distinguished SPAB was observed (Figure 12) upon the titration, due to the aggregation of PL_2-AgNPS@11MUA; again, the titration curves ($Abs_{2ndSPAB}/Abs_{394}$ vs. concentration) were characterized by three different parts, with the intermediate zones presenting higher slope values.

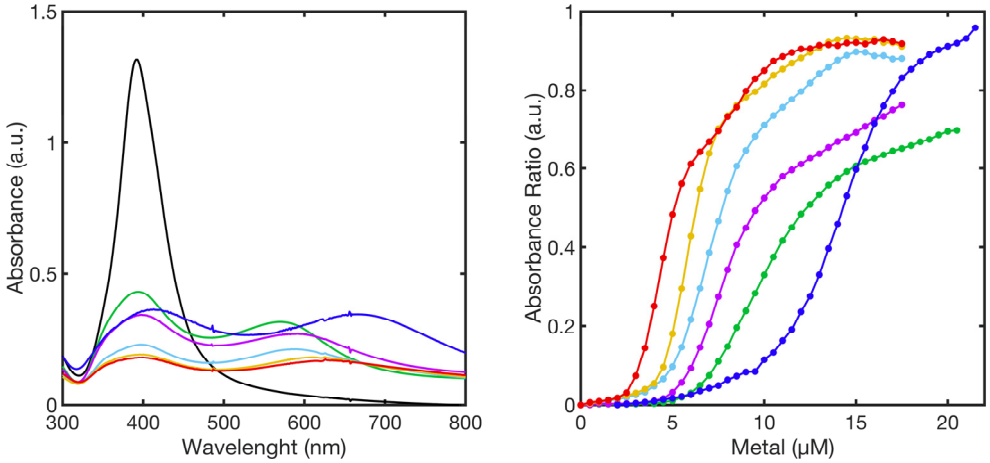

Figure 12. SPABs of PL_2-AgNPs@11MUA (black line) obtained at the highest concentration of metal ions (**left**-panel), calibration curve showing the relationship between absorbance ratio and metal ions concentration used in the titrations (**right**-panel). Ni^{2+} (green line), Mn^{2+} (blue line), Cu^{2+} (red line), Zn^{2+} (cyan line), Co^{2+} (purple line), and Cd^{2+} (yellow line).

In the case of PL_2-AgNPs@11MUA, PCA analysis revealed a general behavior similar to PL_1-AgNPs@11MUA. The scores plot (Figure 13) showed that all metal ions underwent a shift towards higher values, alongside PC1, with increasing metal ion concentrations, due to the decrease in the main SPAB (400 nm) and the appearance of a second SPAB upon aggregation. In line with the titration curves, the shift alongside PC1 was higher in the central zone and its extension was metal-ion dependent. Sample separation alongside PC2 was not so evident, with the sole exclusion of Mn^{2+}, which was unequivocally separated from the other metal ions; this peculiar behavior was likely related to the red shift in the first SPAB at 400 nm (Figure 12, left panel).

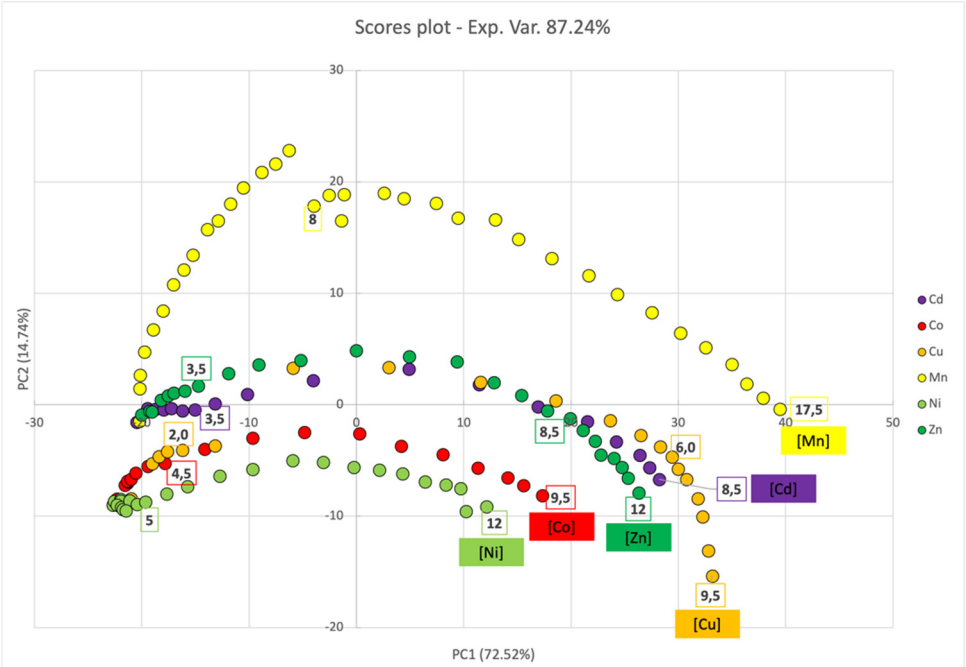

Figure 13. PCA score plot for PC1 and PC2 components upon titration of SPABs of PL_2-AgNPs@11MUA with each metal ion.

4. Conclusions

To dissect the role of coating density in tuning the sensing properties of AgNPs, we produced functionalized silver nanoparticles with different amounts of 11MUA, eventually obtaining multi-layer (ML), full layer (FL), and two partial layers (PL_1 and PL_2) NPs.

Next, the resulting colloidal suspensions were individually titrated with a selection of the most common metal ions present in wastewater (namely, Ni^{2+}, Zn^{2+}, Co^{2+}, Cd^{2+}, Mn^{2+}, and Cu^{2+}) and the consequent variation in SPABs was followed using UV-Vis spectroscopy.

The differently coated AgNPs displayed major differences in their sensing properties. Specifically, multi-layered ML–AgNPs@11MUA did not undergo aggregation upon titration with each metal ion, showing negligible sensing properties. Nevertheless, PCA analysis disclosed a change in the UV-Vis spectra upon titration with metal ions, which was attributed to the interaction between metal ions and the 11MUA on the external layers.

In the case of full-monolayered FL–AgNPs@11MUA, the aggregation of the nanoparticles was triggered upon titration with Ni^{2+} (0.5–10 μM), Mn^{2+}, and Cd^{2+} (0.5–17 μM). Multivariate analysis discriminated metal ions both quantitively and qualitatively. Specifically, Ni^{2+} was evidently separated from the other metal ions, supporting the specific use of FL–AgNPs@11MUA for its detection [13].

The most interesting results in terms of aggregation were observed when the AgNPs were functionalized with partial layers. PL_1-AgNPs@11MUA underwent aggregation upon titration with each metal ion, forming a superlattice of PL_1-AgNPS@11MUA-M and causing characteristic colors for each metal ion. At a lower density of the layer (PL_2-AgNPS@11MUA), we did not observe any substantial change in the sensor behavior; the main difference consisted in the shift of the second SPAB at higher wavelengths, indicating the formation of a different superlattice due to the lower density of functionalized molecules on the AgNP surface. Additionally, the effect of increasing metal-ion concentration and the discrimination between the metal ions was properly rationalized by PCA analysis for PL_1 and PL_2. The use of multivariate analysis, even when only exploiting one of its simplest tools, PCA, was extremely helpful in the interpretation of NP behavior, and could support further developments of these sensors for the simultaneous determinations of metal ions in complex mixtures.

To the best of our knowledge, this study demonstrated for the first time that the density of the functionalizing molecules on the surface of AgNPs is critical in establishing the sensor properties. In fact, by tuning the surface density of the functionalizing agent, it was possible to modulate the selectivity and the application range of the AgNPs@11MUA sensor. Given these promising results, additional studies aimed at further dissecting the role of NP coatings are currently underway.

Supplementary Materials: The following supporting information can be downloaded at: https://www.mdpi.com/article/10.3390/chemosensors10110483/s1, Figures S1–S5: Loading plots.

Author Contributions: Conceptualization, A.R., M.C., R.G. and M.A.; methodology, software, validation, investigation, data curation, A.R., L.R.M., M.Z., L.P., R.B. and M.C.; writing—original draft preparation, A.R. and M.C.; writing—review and editing, A.R., M.C. and L.R.M.; visualization, R.G., M.A., R.B. and M.Z.; supervision, R.G., M.A., R.B. and M.C. All authors have read and agreed to the published version of the manuscript.

Funding: This research received no external funding.

Institutional Review Board Statement: Not applicable.

Informed Consent Statement: Not applicable.

Data Availability Statement: The completed data of this study are available from the corresponding author, upon reasonable request.

Acknowledgments: The authors are grateful to the School of Science and Technology of the University of Camerino for the support and scientific resources such as FE-SEM equipment.

Conflicts of Interest: The authors declare no conflict of interest.

References

1. Hoffman, J.B.; Hennig, B. Protective influence of healthful nutrition on mechanisms of environmental pollutant toxicity and disease risks. *Ann. N. Y. Acad. Sci.* **2017**, *1398*, 99–107. [CrossRef]
2. Mitra, S.; Chakraborty, A.J.; Tareq, A.M.; Emran, T.B.; Nainu, F.; Khusro, A.; Idris, A.M.; Khandaker, M.U.; Osman, H.; Alhumaydhi, F.A.; et al. Impact of heavy metals on the environment and human health: Novel therapeutic insights to counter the toxicity. *J. King Saud Univ. Sci.* **2022**, *34*, 101865. [CrossRef]
3. Thakur, A.; Kumar, A. Recent advances on rapid detection and remediation of environmental pollutants utilizing nanomaterials-based (bio)sensors. *Sci. Total Environ.* **2022**, *834*, 155219. [CrossRef] [PubMed]
4. Prosposito, P.; Burratti, L.; Venditti, I. Silver Nanoparticles as Colorimetric Sensors for Water Pollutants. *Chemosensors* **2020**, *8*, 26. [CrossRef]
5. Lesiak, A.; Drzozga, K.; Cabaj, J.; Bański, M.; Malecha, K.; Podhorodecki, A. Optical sensors based on II-VI quantum dots. *Nanomaterials* **2019**, *9*, 192. [CrossRef]
6. Shen, L.; Chen, M.; Hu, L.; Chen, X.; Wang, J. Growth and Stabilization of Silver Nanoparticles on Carbon Dots and Sensing Application. *Langmuir* **2013**, *29*, 16135–16140. [CrossRef]
7. Jiménez-López, J.; Llorent-Martínez, E.J.; Ortega-Barrales, P.; Ruiz-Medina, A. Graphene quantum dots-silver nanoparticles as a novel sensitive and selective luminescence probe for the detection of glyphosate in food samples. *Talanta* **2020**, *207*, 120344. [CrossRef]
8. Zhu, L.; Feng, X.; Yang, S.; Wang, J.; Pan, Y.; Ding, J.; Li, C.; Yin, X.; Yu, Y. Colorimetric detection of immunomagnetically captured rare number CTCs using mDNA-wrapped single-walled carbon nanotubes. *Biosens. Bioelectron.* **2021**, *172*, 112780. [CrossRef]
9. da Silva, A.D.; Paschoalino, W.J.; Damasceno, J.P.V.; Kubota, L.T. Structure, Properties, and Electrochemical Sensing Applications of Graphene-Based Materials. *ChemElectroChem* **2020**, *7*, 4508–4525. [CrossRef]
10. Hernaez, M. Applications of graphene-based materials in sensors. *Sensors* **2020**, *20*, 3196. [CrossRef]
11. Kumari, S.; Sharma, P.; Yadav, S.; Kumar, J.; Vij, A.; Rawat, P.; Kumar, S.; Sinha, C.; Bhattacharya, J.; Srivastava, C.M.; et al. A Novel Synthesis of the Graphene Oxide-Silver (GO-Ag) Nanocomposite for Unique Physiochemical Applications. *ACS Omega* **2020**, *5*, 5041–5047. [CrossRef]
12. Majdoub, M.; Amedlous, A.; Anfar, Z.; Moussaoui, O. MoS2 nanosheets/silver nanoparticles anchored onto textile fabric as "dip catalyst" for synergistic p-nitrophenol hydrogenation. *Environ. Sci. Pollut. Res.* **2021**, *28*, 64674–64686. [CrossRef]
13. Rossi, A.; Zannotti, M.; Cuccioloni, M.; Minicucci, M.; Petetta, L.; Angeletti, M.; Giovannetti, R. Silver Nanoparticle-Based Sensor for the Selective Detection of Nickel Ions. *Nanomaterials* **2021**, *11*, 1733. [CrossRef]
14. Zannotti, M.; Rossi, A.; Giovannetti, R. SERS activity of silver nanosphere, triangular nanoplates, hexagonal nanoplates and quasi-spherical nanoparticles: Effect of shape and morphology. *Coatings* **2020**, *10*, 288. [CrossRef]
15. Shaban, S.M.; Moon, B.-S.; Kim, D.-H. Selective and sensitive colorimetric detection of p-aminophenol in human urine and paracetamol drugs based on seed-mediated growth of silver nanoparticles. *Environ. Technol. Innov.* **2021**, *22*, 101517. [CrossRef]
16. Sahu, B.; Kurrey, R.; Khalkho, B.R.; Deb, M.K. α-Cyclodextrin functionalized silver nanoparticles as colorimetric sensor for micro extraction and trace level detection of chlorpyrifos pesticide in fruits and vegetables. *Colloids Surf. A Physicochem. Eng. Asp.* **2022**, *654*, 129947. [CrossRef]
17. Sahu, S.; Sharma, S.; Kurrey, R.; Ghosh, K.K. Recent advances on gold and silver nanoparticle-based colorimetric strategies for the detection of different substances and SARS-CoV-2: A comprehensive review. *Environ. Sci. Nano* **2022**, *9*, 3684–3710. [CrossRef]
18. Sener, G.; Uzun, L.; Denizli, A. Colorimetric sensor array based on gold nanoparticles and amino acids for identification of toxic metal ions in water. *ACS Appl. Mater. Interfaces* **2014**, *6*, 18395–18400. [CrossRef] [PubMed]
19. Singh, R.; Mehra, R.; Walia, A.; Gupta, S.; Chawla, P.; Kumar, H.; Thakur, A.; Kaushik, R.; Kumar, N. Colorimetric sensing approaches based on silver nanoparticles aggregation for determination of toxic metal ions in water sample: A review. *Int. J. Environ. Anal. Chem.* **2021**, 1–16. [CrossRef]
20. Vilela, D.; González, M.C.; Escarpa, A. Sensing colorimetric approaches based on gold and silver nanoparticles aggregation: Chemical creativity behind the assay. A review. *Anal. Chim. Acta* **2012**, *751*, 24–43. [CrossRef]
21. Alberti, G.; Zanoni, C.; Magnaghi, L.R.; Biesuz, R. Gold and Silver Nanoparticle-Based Colorimetric Sensors: New Trends and Applications. *Chemosensors* **2021**, *9*, 305. [CrossRef]
22. Chen, H.; Zhang, L.; Hu, Y.; Zhou, C.; Lan, W.; Fu, H.; She, Y. Nanomaterials as optical sensors for application in rapid detection of food contaminants, quality and authenticity. *Sens. Actuators B Chem.* **2021**, *329*, 129135. [CrossRef]
23. Amendola, V.; Pilot, R.; Frasconi, M.; Maragò, O.M.; Iatì, M.A. Surface plasmon resonance in gold nanoparticles: A review. *J. Phys. Condens. Matter* **2017**, *29*, 203002. [CrossRef]
24. Jain, P.K.; Huang, X.; El-Sayed, I.H.; El-Sayed, M.A. Review of some interesting surface plasmon resonance-enhanced properties of noble metal nanoparticles and their applications to biosystems. *Plasmonics* **2007**, *2*, 107–118. [CrossRef]
25. Hou, W.; Cronin, S.B. A review of surface plasmon resonance-enhanced photocatalysis. *Adv. Funct. Mater.* **2013**, *23*, 1612–1619. [CrossRef]
26. Kosuda, K.M.; Bingham, J.M.; Wustholz, K.L.; Van Duyne, R.P.; Groarke, R.J. 4.06—Nanostructures and Surface-Enhanced Raman Spectroscopy. In *Comprehensive Nanoscience and Nanotechnology*, 2nd ed.; Andrews, D.L., Lipson, R.H., Nann, T., Eds.; Academic Press: Oxford, UK, 2016; pp. 117–152.
27. McFarland, A.D.; Van Duyne, R.P. Single silver nanoparticles as real-time optical sensors with zeptomole sensitivity. *Nano Lett.* **2003**, *3*, 1057–1062. [CrossRef]

28. Wang, C.; Luconi, M.; Masi, A.; Fernández, L. *Silver Nanoparticles as Optical Sensors*; Intech: Rijeka, Croatia, 2010; Chapter 12.
29. Pacioni, N.L.; Filippenko, V.; Presseau, N.; Scaiano, J.C. Oxidation of copper nanoparticles in water: Mechanistic insights revealed by oxygen uptake and spectroscopic methods. *Dalton Trans.* **2013**, *42*, 5832–5838. [CrossRef] [PubMed]
30. Paramelle, D.; Sadovoy, A.; Gorelik, S.; Free, P.; Hobley, J.; Fernig, D.G. A rapid method to estimate the concentration of citrate capped silver nanoparticles from UV-visible light spectra. *Analyst* **2014**, *139*, 4855–4861. [CrossRef]
31. Xu, G.; Chen, Y.; Tazawa, M.; Jin, P. Surface Plasmon Resonance of Silver Nanoparticles on Vanadium Dioxide. *J. Phys. Chem. B* **2006**, *110*, 2051–2056. [CrossRef]
32. Ngamchuea, K.; Batchelor-McAuley, C.; Sokolov, S.V.; Compton, R.G. Dynamics of silver nanoparticles in aqueous solution in the presence of metal ions. *Anal. Chem.* **2017**, *89*, 10208–10215. [CrossRef]
33. Loiseau, A.; Zhang, L.; Hu, D.; Salmain, M.; Mazouzi, Y.; Flack, R.; Liedberg, B.; Boujday, S. Core–Shell Gold/Silver Nanoparticles for Localized Surface Plasmon Resonance-Based Naked-Eye Toxin Biosensing. *ACS Appl. Mater. Interfaces* **2019**, *11*, 46462–46471. [CrossRef] [PubMed]
34. Amirjani, A.; Haghshenas, D.F. Ag nanostructures as the surface plasmon resonance (SPR)-based sensors: A mechanistic study with an emphasis on heavy metallic ions detection. *Sens. Actuators B Chem.* **2018**, *273*, 1768–1779. [CrossRef]
35. Ghosh, S.K.; Pal, T. Interparticle Coupling Effect on the Surface Plasmon Resonance of Gold Nanoparticles: From Theory to Applications. *Chem. Rev.* **2007**, *107*, 4797–4862. [CrossRef] [PubMed]
36. Liu, B.; Zhuang, J.; Wei, G. Recent advances in the design of colorimetric sensors for environmental monitoring. *Environ. Sci. Nano* **2020**, *7*, 2195–2213. [CrossRef]
37. Qasem, N.A.A.; Mohammed, R.H.; Lawal, D.U. Removal of heavy metal ions from wastewater: A comprehensive and critical review. *Npj Clean Water* **2021**, *4*, 36. [CrossRef]
38. Bro, R.; Smilde, A.K. Principal component analysis. *Anal. Methods* **2014**, *6*, 2812–2831. [CrossRef]
39. D'Amato, C.A.; Giovannetti, R.; Zannotti, M.; Rommozzi, E.; Minicucci, M.; Gunnella, R.; Di Cicco, A. Band Gap Implications on Nano-TiO2 Surface Modification with Ascorbic Acid for Visible Light-Active Polypropylene Coated Photocatalyst. *Nanomaterials* **2018**, *8*, 599. [CrossRef]
40. Leardi, R.; Polotti, C.M.G. CAT (Chemometric Agile Tool) Freely. Available online: http://gruppochemiometria.it/index.php/software (accessed on 1 September 2022).
41. Zannotti, M.; Vicomandi, V.; Rossi, A.; Minicucci, M.; Ferraro, S.; Petetta, L.; Giovannetti, R. Tuning of hydrogen peroxide etching during the synthesis of silver nanoparticles. An application of triangular nanoplates as plasmon sensors for Hg^{2+} in aqueous solution. *J. Mol. Liq.* **2020**, *309*, 113238. [CrossRef]
42. Hinterwirth, H.; Kappel, S.; Waitz, T.; Prohaska, T.; Lindner, W.; Lämmerhofer, M. Quantifying thiol ligand density of self-assembled monolayers on gold nanoparticles by inductively coupled plasma–mass spectrometry. *ACS Nano* **2013**, *7*, 1129–1136. [CrossRef]
43. Kalishwaralal, K.; BarathManiKanth, S.; Pandian, S.R.K.; Deepak, V.; Gurunathan, S. Silver nanoparticles impede the biofilm formation by Pseudomonas aeruginosa and Staphylococcus epidermidis. *Colloids Surf. B Biointerfaces* **2010**, *79*, 340–344. [CrossRef]
44. Ivanov, M.R.; Bednar, H.R.; Haes, A.J. Investigations of the Mechanism of Gold Nanoparticle Stability and Surface Functionalization in Capillary Electrophoresis. *ACS Nano* **2009**, *3*, 386–394. [CrossRef] [PubMed]
45. Tripathy, S.K.; Yu, Y.-T. Spectroscopic investigation of S–Ag interaction in ω-mercaptoundecanoic acid capped silver nanoparticles. *Spectrochim. Acta Part A Mol. Biomol. Spectrosc.* **2009**, *72*, 841–844. [CrossRef]
46. Haes, A.J.; Zou, S.; Schatz, G.C.; Van Duyne, R.P. Nanoscale Optical Biosensor: Short Range Distance Dependence of the Localized Surface Plasmon Resonance of Noble Metal Nanoparticles. *J. Phys. Chem. B* **2004**, *108*, 6961–6968. [CrossRef]
47. Jennings, G.K.; Laibinis, P.E. Self-Assembled n-Alkanethiolate Monolayers on Underpotentially Deposited Adlayers of Silver and Copper on Gold. *J. Am. Chem. Soc.* **1997**, *119*, 5208–5214. [CrossRef]
48. Love, J.C.; Estroff, L.A.; Kriebel, J.K.; Nuzzo, R.G.; Whitesides, G.M. Self-Assembled Monolayers of Thiolates on Metals as a Form of Nanotechnology. *Chem. Rev.* **2005**, *105*, 1103–1170. [CrossRef] [PubMed]
49. Heriot, S.Y.; Zhang, H.-L.; Evans, S.D.; Richardson, T.H. Multilayers of 4-methylbenzenethiol functionalized gold nanoparticles fabricated by Langmuir–Blodgett and Langmuir–Schaefer deposition. *Colloids Surf. A Physicochem. Eng. Asp.* **2006**, *278*, 98–105. [CrossRef]
50. Taglietti, A.; Diaz Fernandez, Y.A.; Amato, E.; Cucca, L.; Dacarro, G.; Grisoli, P.; Necchi, V.; Pallavicini, P.; Pasotti, L.; Patrini, M. Antibacterial Activity of Glutathione-Coated Silver Nanoparticles against Gram Positive and Gram Negative Bacteria. *Langmuir* **2012**, *28*, 8140–8148. [CrossRef]
51. He, W.; Luo, L.; Liu, Q.; Chen, Z. Colorimetric Sensor Array for Discrimination of Heavy Metal Ions in Aqueous Solution Based on Three Kinds of Thiols as Receptors. *Anal. Chem.* **2018**, *90*, 4770–4775. [CrossRef]
52. Oliveira, C.S.; Nogara, P.A.; Lima, L.S.; Galiciolli, M.E.A.; Souza, J.V.; Aschner, M.; Rocha, J.B.T. Toxic metals that interact with thiol groups and alteration in insect behavior. *Curr. Opin. Insect Sci.* **2022**, *52*, 100923. [CrossRef]
53. Bala, T.; Prasad, B.L.V.; Sastry, M.; Kahaly, M.U.; Waghmare, U.V. Interaction of Different Metal Ions with Carboxylic Acid Group: A Quantitative Study. *J. Phys. Chem. A* **2007**, *111*, 6183–6190. [CrossRef]
54. Laborda, F.; Jiménez-Lamana, J.; Bolea, E.; Castillo, J.R. Selective identification, characterization and determination of dissolved silver(i) and silver nanoparticles based on single particle detection by inductively coupled plasma mass spectrometry. *J. Anal. At. Spectrom.* **2011**, *26*, 1362–1371. [CrossRef]
55. Weiping, C.; Lide, Z. Synthesis and structural and optical properties of mesoporous silica containing silver nanoparticles. *J. Phys. Condens. Matter* **1997**, *9*, 7257–7267. [CrossRef]

56. Si, K.J.; Chen, Y.; Shi, Q.; Cheng, W. Nanoparticle Superlattices: The Roles of Soft Ligands. *Adv. Sci.* **2018**, *5*, 1700179. [CrossRef] [PubMed]